3D Wave-equation Dispersion Inversion of Surface Waves Recorded on Irregular Topography

Zhaolun Liu[1*], *Jing Li*[2] *and Gerard Schuster*[1]
[1] *King Abdullah University of Science and Technology (KAUST),* [2] *Jilin University*

SUMMARY

Irregular topography can cause strong scattering and defocusing of propagating surface waves. Thus it is important to consider such effects when inverting surface waves for the shallow S-velocity structures. We present a 3D surface-wave dispersion inversion method that takes into account the topographic effects modeled by a 3D spectral element solver. The objective function is the frequency summation of the squared wavenumber $\Delta\kappa(\omega)^2$ differences along each azimuth angle of the fundamental or higher modes of Rayleigh waves in each shot gather. Here, the wavenumber $\kappa(\omega)$ associated with the dispersion curve is calculated using the geodesic distance along the irregular free surface. Numerical tests on synthetic data demonstrate that 3D topographic wave equation dispersion inversion (TWD) can accurately invert for the S-velocity model from the dispersion curves computed from the data recorded on irregular topography.

INTRODUCTION

Irregular topography is known to have a significant impact on the amplitudes and phases of propagating surface waves (Snieder, 1986; Fu and Wu, 2001). Ignoring topography in surface wave inversion can lead to significant errors in the inverted model. Moreover, it is expected that 2D assumptions cannot fully approximate wave propagation in the presence of significant 3D variations in topography. In these cases, it is important to employ a 3D surface-wave inversion method that fully accounts for propagation in irregular topography.

When the wavelength is much smaller than the characteristic scale of the topographic relief, the source-receiver distance factor may play a significant role, especially for the fundamental mode of the Rayleigh wave whose propagation is strongly influenced by the free surface (Köhler et al., 2012). Köhler et al. (2012) empirically investigated the effect of topography on the propagation of short-period Rayleigh waves by elastic simulations with a spectral element code and a 3-D model with significant topographical variations. They showed that topography along a profile could result in an underestimation of the phase velocities associated with the surface waves.

Accounting for topography is also essential for full waveform inversion (FWI) of surface waves. Nuber et al. (2016) and Pan et al. (2018) use simulations to demonstrate that even minor topographic variations of the free surface will have a significant effect in FWI. They found that neglecting topography with an amplitude fluctuation greater than half the minimum seismic wavelength leads to significant artifacts in the inverted image (Nuber et al., 2016).

Li and Schuster (2016) developed a wave equation dispersion inversion (WD) method for inverting dispersion curves associated with surface waves. Liu et al. (2018) extended it to the 3D case, which includes the multi-scale and layer-stripping WD proposed by Liu and Huang (2018). Empirical evidence suggests that WD has the benefit of robust convergence compared to the tendency of FWI (Groos et al., 2014; Pérez Solano et al., 2014; Dou and Ajo-Franklin, 2014; Yuan et al., 2015; Groos et al., 2017) to getting stuck in local minima. It has the advantage over the traditional inversion of dispersion curves (Haskell, 1953; Xia et al., 1999, 2002; Park et al., 1999) in that it does not assume a layered model and is valid for arbitrary 2D or 3D media. Li et al. (2019) developed 2D topographic WD (TWD) which incorporates the free-surface topography into the finite-difference solution to the elastic wave equation. Our new paper now extends 2D TWD to the 3D case. To account for strong variations in topography, we use the elastic modeling code SPECFEM3D based on the spectral-element method (SEM) (Komatitsch and Vilotte, 1998; Komatitsch and Tromp, 1999). The inversion algorithm is written in the format of SeisFlows, an open source Python package that can interface with SPECFEM3D (Modrak et al., 2018).

After the introduction, we describe the theory of 3D TWD and its implementation. We also discuss how to calculate the source-receiver offset distance along a 3D irregular surface, which is used to calculate the dispersion curves of the data collected on the irregular surface. Numerical tests on synthetic data are presented in the third section to validate the theory. Finally, the discussion and conclusions are given in the fourth and last sections.

THEORY

We first present the mathematical theory for 3D TWD, following the derivation of Liu et al. (2018), except it is for a 3D irregular surface. Following this, we show how to calculate the source-receiver distance on a 3D irregular surface. Finally, the workflow of 3D TWD is given.

Theory of 3D TWD

The basic theory of 3D TWD is the same as 3D WD (Liu et al., 2018), except a 3D topographic surface is now included in the formulation. The wave-equation dispersion inversion method inverts for the S-wave velocity model to minimize the dispersion objective function

$$\varepsilon = \frac{1}{2}\sum_{\omega}\sum_{\theta}\overbrace{[\kappa(\theta,\omega)_{pre}-\kappa(\theta,\omega)_{obs}]}^{residual=\Delta\kappa(\theta,\omega)}{}^2, \qquad (1)$$

where $\kappa(\omega,\theta)_{pre}$ represents the predicted dispersion curve picked from the simulated spectrum along the azimuth angle θ, and $\kappa(\omega,\theta)_{obs}$ describes the observed dispersion curve obtained from the recorded spectrum along the azimuth θ. In the 2D

10.1190/segam2019-3215009.1

case, the azimuthal angles have only two values: 0° and 180°, corresponding to the left and right directions, respectively.

The gradient $\gamma(\boldsymbol{x})$ of ε with respect to the S-wave velocity $v_s(\boldsymbol{x})$ is given by Liu et al. (2018):

$$\gamma(\boldsymbol{x}) = \frac{\partial \varepsilon}{\partial v_s(\boldsymbol{x})} = -\sum_{\omega} 4 v_{s0}(\boldsymbol{x}) \rho_0(\boldsymbol{x}) \Re \Big\{ \overbrace{\int \sum_{\theta} \frac{1}{A(\theta,\omega)} \Delta\kappa(\theta,\omega) \hat{D}(\boldsymbol{g},\theta,\omega)^*_{obs} G_{3k,k}(\boldsymbol{g}|\boldsymbol{x}) d\boldsymbol{g}}^{backprojected\ data = B_{k,k}(\boldsymbol{x},\omega)^*} \overbrace{D_{j,j}(\boldsymbol{x},\omega)}^{source = f_{j,j}(\boldsymbol{x},\omega)} - \overbrace{\frac{1}{2} \int \sum_{\theta} \frac{1}{A(\theta,\omega)} \Delta\kappa(\theta,\omega) \hat{D}(\boldsymbol{g},\theta,\omega)^*_{obs} G_{3n,k}(\boldsymbol{g}|\boldsymbol{x}) d\boldsymbol{g}}^{backprojected\ data = B_{n,k}(\boldsymbol{x},\omega)^*} \overbrace{\big[D_{k,n}(\boldsymbol{x},\omega) + D_{n,k}(\boldsymbol{x},\omega)\big]}^{source = f_{n,k}(\boldsymbol{x},\omega)} \Big\}, \quad (2)$$

where $v_{s0}(\boldsymbol{x})$ and $\rho_0(\boldsymbol{x})$ are the reference S-velocity and density distributions at location $\boldsymbol{x}$, respectively, and $A(\theta,\omega)$ is given in Liu et al. (2018). $D_i(\boldsymbol{x},\omega)$ denotes the i^{th} component of the particle velocity recorded at $\boldsymbol{x}$ resulting from a vertical-component force. The Einstein notation is assumed in equation 2, where $D_{i,j} = \frac{\partial D_i}{\partial_{x_j}}$ for $i,j \in \{1,2,3\}$. The 3D harmonic Green's tensor $G_{3j}(\boldsymbol{g}|\boldsymbol{x})$ is the particle velocity at location $\boldsymbol{g}$ along the j^{th} direction resulting from a vertical-component source at $\boldsymbol{x}$ in the reference medium. The term $f_{i,j}(\boldsymbol{x},\omega)$ for i and $j \in \{1,2,3\}$ is the downgoing source field at $\boldsymbol{x}$, and $B_{i,j}(\boldsymbol{x},\boldsymbol{s},\omega)$ for i and $j \in \{1,2,3\}$ is the backprojected scattered field at $\boldsymbol{x}$. $\hat{D}(\boldsymbol{g},\theta,\omega)^*_{obs}$ represents the weighted conjugated data defined as

$$\hat{D}(\boldsymbol{g},\theta,\omega)^*_{obs} = 2\pi i \boldsymbol{g}\cdot\boldsymbol{n} e^{i\boldsymbol{g}\cdot\boldsymbol{n}\Delta\kappa} \int_C D(\boldsymbol{g}',\omega)^*_{obs} d\boldsymbol{g}', \quad (3)$$

where $\boldsymbol{n} = (\cos\theta, \sin\theta)$ and C is the line $(\boldsymbol{g}' - \boldsymbol{g})\cdot\boldsymbol{n} = 0$. The above equation indicates that the gradient is computed using a weighted zero-lag correlation between the source and backward-extrapolated receiver wavefields.

The optimal S-wave velocity model $v_s(\boldsymbol{x})$ is obtained using the steepest-descent formula (Nocedal and Wright, 2006)

$$v_s(\boldsymbol{x})^{(k+1)} = v_s(\boldsymbol{x})^{(k)} - \alpha\gamma(\boldsymbol{x}), \quad (4)$$

where α is the step length and the superscript (k) denotes the k^{th} iteration. In practice a preconditoned conjugate gradient method can be used for faster convergence.

Source-receiver Distance on a 3D Irregular Surface

When the wavelength is smaller than the characteristic wavelength of the topographical relief, the source-receiver distance factor may play a significant role. Thus, we should calculate the source-receiver offset distance along the actual irregular surface instead of assuming it to be a flat surface.

For the flat free surface shown in Figure 1a, the source-receiver offset l along the surface is the length of the line segment $\mathbf{sr_1}$, which is the same as the Euclidean distance l_e between the source at $\mathbf{s}$ and the receiver at $\mathbf{r_1}$. When the surface is irregular as shown in Figure 1b, the source-receiver offset l along the surface is the length of the segment of a curve on the surface, which is larger than the Euclidean distance l_e. The source-receiver offset distance along the irregular surface is called the "geodesic distance", which is the shortest route between two points on the surface.

Figure 2 shows the offset L and azimuth θ from the source at $\mathbf{s}$ to the receiver at $\mathbf{r}$ on an irregular surface. Here, the azimuth is along the direction from $\mathbf{s}'$ to $\mathbf{r}'$, where $\mathbf{s}'$ and $\mathbf{r}'$ are the projections of points $\mathbf{s}$ and $\mathbf{r}$ on the plane $z = 0$, respectively. Once we get the offset and azimuth for the receivers, we can calculate the dispersion curve of the data by the discrete Radon transform in the frequency domain.

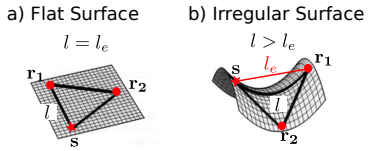

Figure 1: Schematic diagram shows the offset distance l along the (a) flat and (b) irregular surfaces from the source at $\mathbf{s}$ (the red star) to the receiver at $\mathbf{r_1}$, where l_e is the Euclidean distance.

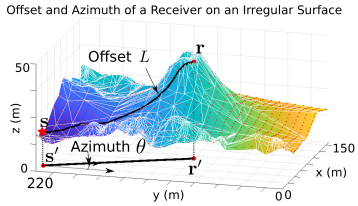

Figure 2: Schematic diagram shows the offset L and the azimuth θ from the source at $\mathbf{s}$ (red star) to the receiver at $\mathbf{r}$.

Workflow of 3D TWD

The workflow for implementing 3D TWD is summarized in the following steps.

1. Remove the first-arrival body waves and higher-order modes of the Rayleigh waves in the shot gathers (Li et al., 2017).
2. Determine the source-receiver offset along the irregular surface, and the range of the dominant azimuth angles θ for each shot gather.
3. Apply a discrete Radon transform followed by the temporal Fourier transform of the predicted and observed common shot gathers (CSGs) to compute the dispersion curves $\kappa(\theta,\omega)$ and $\kappa(\theta,\omega)_{obs}$ along each azimuth angle θ. Calculate the sum of the squared dispersion residuals in equation 1.
4. Calculate the weighted data $\hat{D}(\boldsymbol{g},\omega)^*_{obs}$ according to equation 3. The source-side and receiver-side wavefields in equation 2 are computed by the SEM solution to the 3D elastic wave equation.

10.1190/segam2019-3215009.1

5. Calculate and sum the gradients for all the shot gathers. Source illumination is sometimes needed as a preconditioner (Plessix and Mulder, 2004).
6. Calculate the step length and update the S-wave tomogram using the steepest-descent or conjugate gradient methods. In practice, we use a preconditoned conjugate gradient method.

NUMERICAL RESULTS

The effectiveness of 3D TWD is evaluated with the 3D Foothills model. The observed and predicted data are generated by a spectral-element solver SPECFEM3D (Komatitsch and Vilotte, 1998; Komatitsch and Tromp, 1999). The mesh is generated by the software package CUBIT. For 3D TWD, only the S-wave velocity model is inverted and the true P-wave velocity model is used for modeling the predicted surface waves. The density model is homogeneous with ρ =2000 kg/m^3. The source wavelet is a Ricker wavelet for the synthetic data.

The topography of the 3D Foothills model shown in Figure 3 is extracted from the 3D SEG Advanced Modeling (SEAM) phase II foothills model (Oristaglio, 2012), where the red lines are the geodesic paths on the triangular mesh for the source marked as the red star. The maximum elevation difference of the topography is 1.2 km. The 3D Foothills S-wave velocity model shown in Figure 4a is modified from the 2D Foothills model in Figure 2a of Brenders et al. (2008). The P-wave velocity is defined as $v_p = \sqrt{3}v_s$ and the physical size of the velocity model is 7 km and 3.5 km in the x and y directions, respectively, and is 2 km deep in the z-direction. The mesh used in the SPECFEM3D is shown in Figure 4b. The initial S-velocity model is shown in Figure 4c. Figure 5 shows the acquisition geometry for this experiment, where 2312 geophones are distributed on the surface, which are arranged in 17 parallel lines along the x-direction, and each line has 136 receivers. The in-line and cross-line receiver intervals are 50 m and 190 m, respectively. There are 80 vertical-component shots distributed on a 10×8 grid with source intervals of 750 m and 380 m in the x and y directions, respectively. The peak frequency of the source is 5 Hz and the observed data are recorded for 2.40 seconds with a 0.8 ms sampling rate.

The fundamental dispersion curves for each CSG are picked for the frequencies from 2 to 9 Hz along the dominant azimuths from 0° to 360° with an interval of 5°. For example, Figure 6 shows the observed dispersion curves calculated from the CSGs for the sources located at points A, B, C and D indicated in Figure 5, where the black dashed lines represent the contours of the observed dispersion curves. The cyan lines represent the contours of initial dispersion curves.

3D TWD is then used to invert for the S-velocity distributions. Figure 4d displays the inverted S-wave velocity model. The vertical slices for the true, initial and inverted models are shown in Figures 7a, 7b and 7c, respectively, where the black- and white- dashed lines indicate the large velocity contrast boundaries and the boundaries 0.5 km below the free surface, respectively. The depth slices 300 m below the free surface for the true, initial and inverted models are shown in Figures 8a, 8b and 8c, respectively. We can see that the S-velocity model is significantly updated in the shallow part, where most updates are confined to the region within 0.5 km from the surface. The overall velocity structure is well recovered, even though some small-scale features are still missing, which might be caused by the limited frequency content.

The contours of the predicted dispersion curves for the sources located at points A, B, C and D in Figure 5 are represented by the red dash-dot lines in Figure 6, which agree with the contours of the observed dispersion curves. Figure 9 compares the observed (red) and synthetic (blue) traces at the far source-receiver offsets predicted from the initial and inverted models for (a) and (b) with CSG at B, and (c) and (d) with CSG at C. It can be seen that the synthetic waveforms computed from the 3D TWD tomogram closely agree with the observed ones.

CONCLUSIONS

We present the 3D TWD method that accounts for an irregular recording surface. The effectiveness of this method is numerically demonstrated with synthetic data recorded on an irregular free surface. The main limitation of 3D WD is its high computational cost, which is more than an order-of-magnitude greater than that of 2D WD. However, the improvement in accuracy compared to 2D WD can sometimes make this extra cost worthwhile when there are significant near-surface lateral variations in the S-velocity distribution.

ACKNOWLEDGEMENTS

The research reported in this publication was supported by the King Abdullah University of Science and Technology (KAUST) in Thuwal, Saudi Arabia. We are grateful to the sponsors of the Center for Subsurface Imaging and Modeling Consortium for their financial support. For computer time, this research used the resources of the Supercomputing Laboratory at KAUST and the IT Research Computing Group. We thank them for providing the computational resources required for carrying out this work.

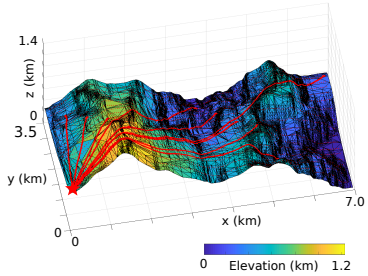

Figure 3: Triangle mesh for the topography of the 3D Foothill model, where the red lines are the geodesic paths for the source marked as the red star.

10.1190/segam2019-3215009.1

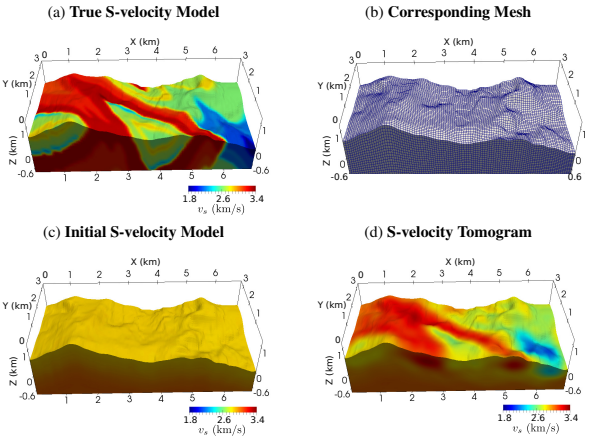

Figure 4: (a) True S-velocity model, (b) corresponding mesh, (c) initial S-velocity model and (d) S-velocity tomogram.

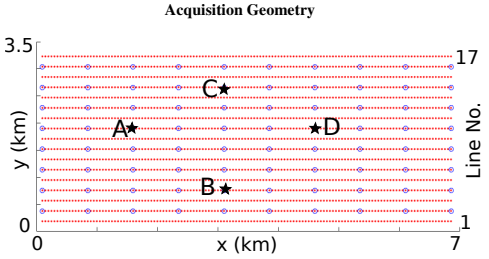

Figure 5: Acquisition geometry for the numerical tests with data generated for the 3D Foothill model, where the red dots and blue circles indicate the locations of the receivers and sources, respectively.

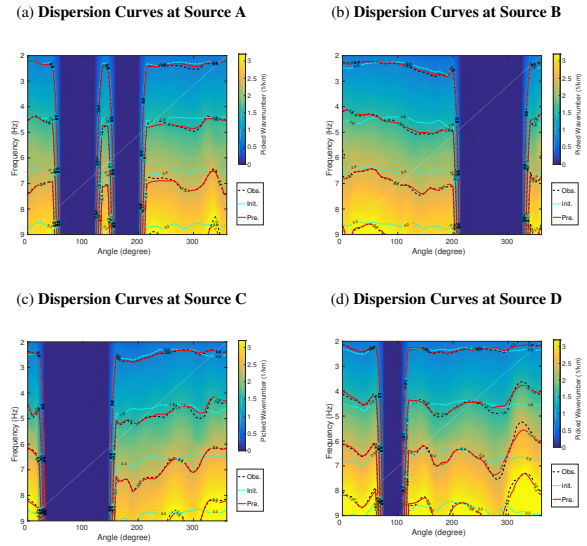

Figure 6: Observed dispersion curves for the sources located at (a) A, (b) B, (c) C and (d) D indicated in Figure 5b, where the black dashed lines, the cyan dash-dot lines and the red lines represent the contours of the observed, initial and inverted dispersion curves, respectively.

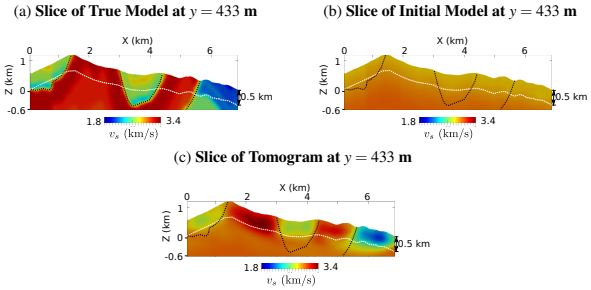

Figure 7: Slices of the (a) true, (b) initial, and (c) inverted S-velocity models at y = 433 m, where the black and white dashed lines indicate the large velocity contrast boundaries and the boundaries 0.5 km below the free surface, respectively.

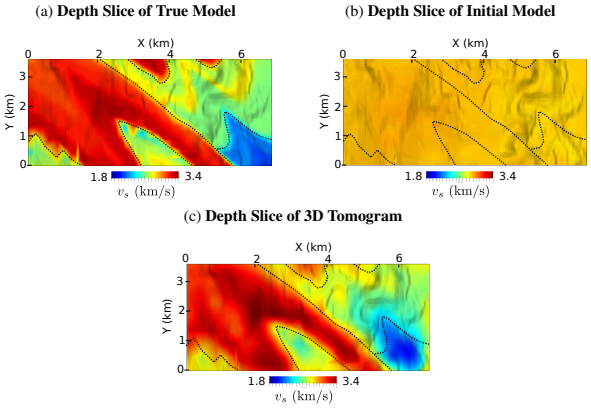

Figure 8: Depth slices 300 m below the surface for the (a) true, (b) initial and (c) inverted Foothill S-velocity models.

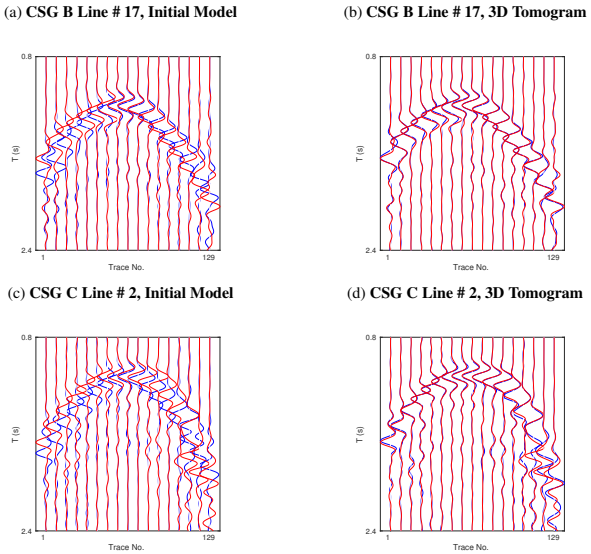

Figure 9: Comparison between the observed (red) and synthetic (blue) traces at far offsets predicted from the initial model (LHS panels) and 3D tomogram (RHS panels) for CSG B in (a) and (b), and CSG C in (c) and (d). Here, the locations of points B and C and the line number are indicated in Figure 5.

10.1190/segam2019-3215009.1

REFERENCES

Brenders, A., S., Charles, and R., Pratt, 2008, Velocity estimation by waveform tomography in the Canadian Foothill-a synthetic benchmark study: 70th Annual International Conference and Exhibition, EAGE, Extended Abstracts, doi: https://doi.org/10.3997/2214-4609.20147678.

Dou, S., and J. B., Ajo-Franklin, 2014, Full-wavefield inversion of surface waves for mapping embedded low-velocity zones in permafrost: Geophysics, **79**, no. 6, EN107–EN124, doi: https://doi.org/10.1190/geo2013-0427.1.

Fu, L.-Y., and R.-S., Wu, 2001, A hybrid BE-GS method for modeling regional wave propagation: Pure and Applied Geophysics, **158**, 1251–1277, doi: https://doi.org/10.1007/PL00001222.

Groos, L., M., Schäfer, T., Forbriger, and T., Bohlen, 2014, The role of attenuation in 2D full-waveform inversion of shallow-seismic body and Rayleigh waves: Geophysics, **79**, no. 6, R247–R261, doi: https://doi.org/10.1190/geo2013-0462.1.

Groos, L., M., Schäfer, T., Forbriger, and T., Bohlen, 2017, Application of a complete workflow for 2D elastic full-waveform inversion to recorded shallow-seismic Rayleigh waves: Geophysics, **82**, no. 2, R109–R117, doi: https://doi.org/10.1190/geo2016-0284.1.

Haskell, N. A., 1953, The dispersion of surface waves on multilayered media: Bulletin of the Seismological Society of America, **43**, 17–34.

Köhler, A., C., Weidle, and V., Maupin, 2012, On the effect of topography on surface wave propagation in the ambient noise frequency range: Journal of Seismology, **16**, 221–231, doi: https://doi.org/10.1007/s10950-011-9264-5.

Komatitsch, D., and J., Tromp, 1999, Introduction to the spectral element method for three-dimensional seismic wave propagation: Geophysical Journal International, **139**, 806–822, doi: https://doi.org/10.1046/j.1365-246x.1999.00967.x.

Komatitsch, D., and J.-P., Vilotte, 1998, The spectral element method: An efficient tool to simulate the seismic response of 2D and 3D geological structures: Bulletin of the Seismological Society of America, **88**, 368.

Li, J., Z., Feng, and G., Schuster, 2017, Wave-equation dispersion inversion: Geophysical Journal International, **208**, 1567–1578, doi: https://doi.org/10.1093/https://doi.org/gjihttps://doi.org//ggw465.

Li, J., F.-C., Lin, A., Allam, Y., Ben-Zion, Z., Liu, and G., Schuster, 2019, Wave equation dispersion inversion of surface waves recorded on irregular topography: Geophysical Journal International, **217**, 346–360, doi: https://doi.org/10.1093/https://doi.org/gjihttps://doi.org//ggz005.

Li, J., and G., Schuster, 2016, Skeletonized wave equation of surface wave dispersion inversion: 86th Annual International Meeting, SEG, Expanded Abstracts, 3630–3635, doi: https://doi.org/10.1190/segam2016-13770057.1.

Liu, Z., and L., Huang, 2018, Multiscale and layer-stripping wave-equation dispersion inversion of Rayleigh waves: 88th Annual International Meeting, SEG, Expanded Abstracts, 2536–2540, doi: https://doi.org/10.1190/segam2018-2997500.1.

Liu, Z., J., Li, S. M., Hanafy, and G. T., Schuster, 2018, 3D wave-equation dispersion inversion of surface waves: 88th Annual International Meeting, SEG, Expanded Abstracts, 4733–4737, doi: https://doi.org/10.1190/geo2018-0543.1.

Modrak, R. T., D., Borisov, M., Lefebvre, and J., Tromp, 2018, Seisflows-flexible waveform inversion software: Computers and Geosciences, **115**, 88–95, doi: https://doi.org/10.1016/j.cageo.2018.02.004.

Nocedal, J., and S., Wright, 2006, Numerical optimization: Springer Science and Business Media.

Nuber, A., E., Manukyan, and H., Maurer, 2016, Ground topography effects on near-surface elastic full waveform inversion: Geophysical Journal International, **207**, 67–71, doi: https://doi.org/10.1093/https://doi.org/gjihttps://doi.org//ggw267.

Oristaglio, M., 2012, Seam update: The Leading Edge, **31**, 1130–1132, doi: https://doi.org/10.1190/tle31101130.1.

Pan, Y., L., Gao, and T., Bohlen, 2018, Time-domain full-waveform inversion of Rayleigh and Love waves in presence of free-surface topography: Journal of Applied Geophysics, **152**, 77–85, doi: https://doi.org/10.1016/j.jappgeo.2018.03.006.

Park, C. B., R. D., Miller, and J., Xia, 1999, Multichannel analysis of surface waves: Geophysics, **64**, 800–808, doi: https://doi.org/10.1190/1.1444590.

Pérez Solano, C. A., D., Donno, and H., Chauris, 2014, Alternative waveform inversion for surface wave analysis in 2-D media: Geophysical Journal International, **198**, 1359–1372, doi: https://doi.org/10.1093/https://doi.org/gjihttps://doi.org//ggu211.

Plessix, R.-E., and W., Mulder, 2004, Frequency-domain finite-difference amplitude-preserving migration: Geophysical Journal International, **157**, 975–987, doi: https://doi.org/10.1111/gji.2004.157.issue-3.

Snieder, R., 1986, The influence of topography on the propagation and scattering of surface waves: Physics of the Earth and Planetary Interiors, **44**, 226–241, doi: https://doi.org/10.1016/0031-9201(86)90072-5.

Xia, J., R., Miller, C., Park, and G., Tian, 2002, Determining Q of near-surface materials from Rayleigh waves: Journal of Applied Geophysics, **51**, 121–129, doi: https://doi.org/10.1016/S0926-9851(02)00228-8.

Xia, J., R. D., Miller, and C. B., Park, 1999, Estimation of near-surface shear-wave velocity by inversion of Rayleigh waves: Geophysics, **64**, 691–700, doi: https://doi.org/10.1190/1.1444578.

Yuan, Y. O., F. J., Simons, and E., Bozdağ, 2015, Multiscale adjoint waveform tomography for surface and body waves: Geophysics, **80**, no. 5, R281–R302, doi: https://doi.org/10.1190/geo2014-0461.1.